



HAL
open science

Algal Remodeling in a Ubiquitous Planktonic Photosymbiosis

Johan Decelle, Hryhoriy Stryhanyuk, Benoit Gallet, Giulia Veronesi, Matthias Schmidt, Sergio Balzano, Sophie Marro, Clarisse Uwizeye, Pierre-Henri Jouneau, Josselin Lupette, et al.

► **To cite this version:**

Johan Decelle, Hryhoriy Stryhanyuk, Benoit Gallet, Giulia Veronesi, Matthias Schmidt, et al.. Algal Remodeling in a Ubiquitous Planktonic Photosymbiosis. *Current Biology - CB*, 2019, 29 (6), pp.968-978.e4. 10.1016/j.cub.2019.01.073 . hal-02083159

HAL Id: hal-02083159

<https://hal.science/hal-02083159>

Submitted on 23 Nov 2020

HAL is a multi-disciplinary open access archive for the deposit and dissemination of scientific research documents, whether they are published or not. The documents may come from teaching and research institutions in France or abroad, or from public or private research centers.

L'archive ouverte pluridisciplinaire **HAL**, est destinée au dépôt et à la diffusion de documents scientifiques de niveau recherche, publiés ou non, émanant des établissements d'enseignement et de recherche français ou étrangers, des laboratoires publics ou privés.

Algal remodeling in a ubiquitous planktonic photosymbiosis

Johan Decelle^{1,10*}, Hryhoriy Stryhanyuk¹, Benoit Gallet², Giulia Veronesi^{3,4}, Matthias Schmidt¹, Sergio Balzano⁵, Sophie Marro⁶, Clarisse Uwizeye⁷, Pierre-Henri Jouneau⁸, Josselin Lupette⁷, Juliette Jouhet⁷, Eric Maréchal⁷, Yannick Schwab⁹, Nicole L. Schieber⁹, Rémi Tucoulou⁴, Hans Richnow¹, Giovanni Finazzi⁷, Niculina Musat¹

1- Helmholtz Centre for Environmental Research – UFZ, Department of Isotope Biogeochemistry, Leipzig, Germany

2- Institut de Biologie Structurale, Université Grenoble Alpes, CNRS, CEA; 71, Avenue des Martyrs, 38044 Grenoble, France

3- Laboratoire de Chimie et Biologie des Métaux UMR 5249, Université Grenoble Alpes, CNRS, CEA; 17, Avenue des Martyrs, 38054 Grenoble, France

4- ESRF, The European Synchrotron Radiation Facility, 71, Avenue des Martyrs, 38043 Grenoble, France

5- NIOZ, Royal Netherlands Institute for Sea Research, Department of Marine Microbiology and Biogeochemistry, and Utrecht University. P.O. Box 59, NL-1790 AB Den Burg, The Netherlands

6- Sorbonne Universités, UPMC Université Paris 06, CNRS, Laboratoire d’Océanographie de Villefranche (LOV) UMR7093, Observatoire Océanologique, 06230 Villefranche-sur-Mer, France

7- Laboratoire de Physiologie Cellulaire et Végétale, Université Grenoble Alpes, CNRS, CEA, INRA; 38054, Grenoble Cedex 9, France

8- Institut Nanosciences et Cryogénie, Université Grenoble Alpes, CEA, F38054 Grenoble, France

9- Cell Biology and Biophysics Unit, European Molecular Biology Laboratory (EMBL), 69117 Heidelberg, Germany

10-Lead contact

*Correspondence: johan.decelle@univ-grenoble-alpes.fr

Summary

Photosymbiosis between single-celled hosts and microalgae is common in oceanic plankton, especially in oligotrophic surface waters. However, the functioning of this ecologically important cell-cell interaction and the subcellular mechanisms allowing the host to accommodate and benefit from its microalgae remain enigmatic. Here, using a combination of quantitative single-cell structural and chemical imaging techniques (FIB-SEM, nanoSIMS, Synchrotron X-ray fluorescence), we show that the structural organization, physiology and trophic status of the algal symbionts (the haptophyte *Phaeocystis*) significantly change within their acantharian hosts compared to their free-living phase in culture. In symbiosis, algal cell division is blocked, photosynthesis is enhanced, and cell volume increases up to 10-fold with a higher number of plastids (from 2 to up to 30) and thylakoid membranes. The multiplication of plastids can lead to a 38-fold increase of the total plastid volume in a cell. Subcellular mapping of nutrients (nitrogen and phosphorous) and their stoichiometric ratios show that symbiotic algae are impoverished in phosphorous and suggest higher investment into energy-acquisition machinery rather than growth. Nanoscale imaging also showed that the host supplies a substantial amount of trace metals (e.g. iron and cobalt), which are stored in algal vacuoles at high concentration (up to 660 ppm). Sulfur mapping reveals a high concentration in algal vacuoles that may be a source of antioxidant

molecules. Overall, this study unveils an unprecedented morphological and metabolic transformation of microalgae following their integration into a host, and suggests that this widespread symbiosis is a farming strategy whereby the host engulfs and exploits microalgae.

Keywords: symbiosis, plankton, microalga, single-cell imaging, photosynthesis, mass spectrometry imaging, 3D electron microscopy

Introduction

Acquisition of plastids by eukaryotic host cells via endosymbiosis with microalgae is heralded as one of the most important biological innovations [1,2]. Prior to genetic integration, hosts had strong control over their photosynthetic symbionts by driving metabolic integration [3,4]. In today's oceanic plankton, living in symbiosis with microalgae (photosymbiosis) is a widespread and ecologically important phenomenon [5,6]. The widely distributed photosymbiosis between heterotrophic radiolarian hosts and eukaryotic microalgae is abundant in surface oligotrophic waters [5,7–9]. These organisms significantly contribute to planktonic biomass, carbon fixation (through photosynthesis of the algal symbionts), and carbon export to the deep ocean [9–12], making them important components of oceanic ecosystems. Photosymbiosis may become even more prominent in the oceans of the future since oligotrophic provinces are expanding due to global warming [13]. While knowledge of the diversity of eukaryotic photosymbioses has greatly improved in the past decade (e.g. radiolarians, foraminiferans) [7,14], their physiology and metabolism remain largely unexplored, as does their biogeochemical significance in marine ecosystems. In particular, investigating the structural and metabolic strategies that allow host cells to integrate and control intracellular microalgae has been a major challenge due to the highly complex nature of their intertwined partnerships, the lack of stable cultures, and the scarcity of knowledge about their genomes and protein functions [15,16]. In the ecologically successful symbiosis between Acantharia (radiolarian host) and the microalga *Phaeocystis*, the host depends entirely on engulfed symbiotic microalgae for growth and survival (i.e., obligatory symbiosis) [7]. By contrast, the microalga *Phaeocystis*, which is a keystone phytoplankton taxon that shapes the structure and function of marine ecosystems, can exist in free-living forms in the environment [17,18]. Phylogenetic analyses including different nuclear and plastidial genes suggest that the free-living and symbiotic *Phaeocystis* populations are genetically identical in a given oceanic region (e.g. *Phaeocystis cordata* in the Mediterranean Sea [7]). Living with the locally adapted and abundant symbiont genotypes would be an advantageous strategy for acantharian hosts that must re-establish the symbiotic partnership at each generation (i.e., horizontal transmission).

We studied this ubiquitous symbiotic interaction between single-celled organisms, which represents a promising model to study the cellular integration of algae into a host and therefore to elucidate the possible processes underpinning plastid acquisition in eukaryotes. We used a combination of 3D electron microscopy, nanoscale mass spectrometry and X-ray fluorescence imaging to investigate the transition between free-living and symbiotic stages of the microalgae at the subcellular level, and disentangle the role of each symbiotic partner. These techniques were complemented by physiological analyses to offer a comprehensive picture of the physiology and metabolism of the interaction. We showed that, within their host, division of algal cells is blocked, and their ultrastructure, physiology and trophic state significantly change, transforming them into a highly productive photosynthetic machinery. This algal remodeling, presumably induced by the host, suggests that this widespread and abundant symbiosis could represent an algal farming strategy, providing a new paradigm for the ecological success of planktonic photosymbiosis in the oligotrophic oceans.

Results and Discussion

Major structural transformation of symbiotic microalgae for enhanced photosynthesis

We investigated the ultrastructure of microalgal symbionts (*Phaeocystis cordata*) within their acantharian hosts (Figure 1A), collected from marine surface waters, and of their free-living phase (i.e. grown *ex hospite* in culture). To preserve their native ultrastructure and chemical composition, cells were cryofixed with high pressure freezing, subjected to freeze substitution and embedded in resin. Transmission electron microscopy of ultrathin sections showed that the free-living microalgae were 3-5 μm in size and typically possessed two parietal plastids (Figure 1B), as described in the taxonomic diagnosis of the species [19]. In stark contrast, the symbiotic microalgae were substantially larger (8-10 μm in size), with average volumes up to 10-fold larger than those of the free-living cells. In addition to a nucleus, symbiotic microalgae possessed up to 31 pyrenoid-containing plastids, located predominantly at the periphery of the cells (Figure 1). Three-dimensional subcellular reconstruction showed the multiple inter-connected plastids occupied most of the algal cell volume and were 3-fold more voluminous than plastids in the free-living microalgae (Figure 1D-E, Figure S1, Video S1). In a single algal cell, our morphometric analyses based on 3D models revealed a 30-fold increase of the total surface of plastids (from 8.4 μm^2 in free-living to 251.6 μm^2 in symbiosis) and a 38-fold increase of the total volume of plastids (from 1 μm^3 in free-living to 38.6 μm^3 in symbiosis). In addition, the plastids of symbiotic microalgae contained far denser networks of stacked thylakoid membranes (17 nm thick), which occupied 64% ($\pm 9\%$) of the plastid surface area compared to 47% ($\pm 13\%$) in the free-living microalgae (Figure 1C). Thus, microalgae in symbiosis significantly expand their photosynthetic surfaces by multiplication of voluminous plastids (from 2 to 31) and thylakoid membranes.

To our knowledge, this significant morphological transformation of the photosynthetic machinery has not been reported in other symbiotic algae from terrestrial and marine ecosystems, such as in coral and other planktonic symbioses [20,21]. To test whether photosynthetic activity is affected by these morphological changes, we conducted *in vivo* photophysiology measurements based on measurements of chlorophyll fluorescence in the free-living and symbiotic microalgae. We found that the electron transfer rate (ETR), a widely used parameter to assess photosynthetic efficiency [22], was significantly higher (up to three times) in the symbiotic microalgae than in the free-living microalgae (Figure 1F). Within the host, photosynthesis was enhanced in a range of light conditions (29 to 672 $\mu\text{mol photons m}^{-2} \text{s}^{-1}$) encompassing values experienced by these organisms in the natural environment [23]. Based on the photosynthesis (ETR) –irradiance curves, different parameters of free-living and symbiotic microalgae were evaluated, such as the maximum photosynthetic capacity (P_m), the photosynthetic efficiency under light levels close to zero (the initial slope α), and the minimum photosynthetic saturation irradiance (E_k) [24]. Compared to free-living, we found higher values of P_m (128.85 ± 6.5 vs 41.34 ± 0.87), α (0.61 ± 0.04 vs 0.40 ± 0.02) and E_k (211.50 ± 16.32 vs 103.12 ± 6.03) in symbiotic microalgae, suggesting that the photosynthetic activity at limiting and saturating light levels was enhanced in symbiosis (Table S1). More particularly, we can conclude that light capture at limiting light was higher in symbiosis

(1.5 times more), as well as carbon assimilation at saturating light (3.1 times more). In addition, excess light dissipation via non-photochemical quenching (NPQ) was diminished in symbiotic microalgae in high light conditions (Figure S2). This suggests that symbiotic microalgae were less exposed to excess light stress, confirming that the environment provided by the host is optimum for their photosynthesis.

High nitrogen and low phosphorous conditions in symbiotic microalgae

The structural and associated physiological changes of symbionts may be promoted by the host to maximize photosynthetic capacity and thereby fully benefit from the photosynthates, such as sugars. The transformed microalgal cells are maintained in an intracellular vacuole (symbiosome, Figure 1), where the host has to provide essential nutrients (nitrogen, phosphorous and trace metals), which generally limit primary productivity of phytoplankton in oceanic waters [25]. In order to highlight possible metabolic changes induced by symbiosis, we investigated the subcellular distribution and composition of nutrients in free-living and symbiotic microalgae. Note that we hereafter compared algal cells grown in an artificial culture medium (free-living condition) and algal cells maintained in the micro-habitat provided by their host (Table S2).

The nitrogen (N) to phosphorus (P) ratio is generally considered a proxy for the metabolic investment of a cell [26]. Depending on environmental factors, microalgal cells are able to differentially allocate N and P into either energy-acquisition machinery (N-rich proteins: high N/P ratio) or growth machinery (P-rich RNA: low N/P ratio) [27,28]. To reconstitute N/P ratios in host cells, symbiotic microalgae and free-living microalgae, we mapped the content and distribution of N and P at a subcellular level using nanoSIMS. In order to compare the relative N and P content between host, symbiotic and free-living microalgae, the total ions counts of these elements were normalized by the total ions counts of carbon (C_2). We showed that symbionts have higher N/P ratios than their hosts (Figure 2C; Data S1), due to a higher N content of the plastids ($p < 0.05$; ANOVA, Figure 2A, Data S1), and a lower cellular P content (Figure 2B). P in symbionts was mainly contained in the nucleus with no evidence of cellular storage (Figure 2B). By contrast, the host cells contained cytosolic hotspots of P, where the content was three- and ten-fold higher than that in the nucleus and plastids of the symbionts, respectively. Overall, N/P ratio mapping in cells suggests the existence of an optimal metabolic coupling and labour division between host (investment in growth) and symbionts (investment in energy-acquisition), which likely provides a competitive edge in resource-limited oceanic waters, like in the Mediterranean Sea.

Compared to free-living cells, the N/P ratios of the symbiotic microalgae were 2-fold higher, especially in plastids ($p = 0.002$, ANOVA; Figure 2I). This was mainly caused by the lower P content of the plastids in the symbionts, since the N content was comparable in plastids of symbiotic and free-living cells ($p > 0.01$, ANOVA; Figure 2 G-I). The P content in symbiotic microalgae could be two times lower than that of free-living cells, and the plastids exhibited a significantly low P content with respect to the cytosol ($p < 0.05$; ANOVA; Figure 2B,E). By contrast, in free-living cells, P was homogeneously distributed and did not exhibit a lower concentration in the plastids (Figure 2E; Data S1). As the non-storage P in algae is mainly

contained in RNA, followed by DNA and phospholipids [29,30], subcellular P mapping suggests that these molecules were present in lower concentration in symbiotic *versus* free-living microalgae. This could result from the increased primary productivity of the symbiotic microalgae that must adjust their nutrient homeostasis and/or from a lower availability of P in the symbiosome compared to the culture medium (Table S2). We can hypothesize that the lower P content in symbiosis could reflect a limitation imposed by the host to control the symbiont population, as observed in reef photosymbioses [31,32]. Under P limitation, cell division is blocked but carbon fixation is maintained in some microalgae [33], which could be an optimal metabolic strategy for the host. Consistent with this hypothesis, we did not observe any *Phaeocystis* cell divisions within their hosts, either from electron micrographs or by *in vivo* monitoring of isolated host cells over 7 days (Figure S3), whereas *Phaeocystis* cells in culture can divide every 6-7 hours [34]. Inorganic P is scarce in oceanic waters, particularly in the Mediterranean Sea [35], and the association with symbiotic microalgae with naturally low phosphate requirements could be a selective pressure for the host. ToF-SIMS molecular mapping of PO_2^- and PO_3^- , which are characteristic phospholipid fragments [36], showed that the phospholipids were barely present in the plastids of the symbiotic microalgae (Figure 3B). Consistent with this finding, our lipidomics analyses revealed that free-living *Phaeocystis* cells, maintained in culture medium where P was not limiting, contained an extremely low quantity of phospholipids. In plastids, their thylakoid membranes consist mainly of non-phosphorous galactolipids (MGDG and DGDG), and their extra-plastidial membranes are mainly composed of the non-phosphorus and N-containing betaine lipids (DGTA and DGCC) (Figure 3C). In *Phaeocystis*, P requirements for thylakoid lipid synthesis and high photosynthetic activity are therefore very low, which is highly advantageous for a host to accommodate a high number of plastids in an oligotrophic environment. Yet, in order to sustain the enhanced primary productivity of its intracellular symbionts, the host must also deliver trace metals, such as iron, which are driving photosynthesis in the oceans [25,37].

Altered metal homeostasis in symbiotic microalgae

Trace metals are essential for photosynthesis, N assimilation, antioxidant protection, and other essential biochemical functions of microalgae [37,38]. The ecological success of the host-symbiont association must therefore rely on efficient mechanisms to uptake, sequester and regulate the exchange of these extremely low-concentrated nutrients in the ocean. Here, we imaged and quantified the subcellular distribution of metals in host and symbiont cells with Synchrotron X-ray fluorescence. We found that the concentration of Fe in symbiotic microalgae was twice as high (90 ± 23 ppm) as that in free-living microalgae (44 ± 6 ppm) (Figure 4, Table S3). The higher concentration of Fe in symbiotic microalgae was mainly due to the presence of large Fe-rich vacuoles in the algal cytosol containing up to 660 ppm Fe (420 ± 210 ppm on average) (Figure 4B-C, Figure S4, Table S4). The same type of vacuoles was also present in free-living microalgae, but they were smaller and approximately 2-fold less concentrated in Fe (160 ± 30 ppm) (Figure 4A,F, Table S4). The individual plastids of free-living and symbiotic *Phaeocystis* cells had similar Fe concentrations. Since they possess large storage vacuoles and numerous plastids, symbiotic

microalgal cells contained substantially more Fe (from 0.77 to 5.50 fg calculated from the analysed surface area), than free-living cells (0.25 ± 0.03 fg). This implies that a significant quantity of Fe is delivered by the host, and once sequestered in the intracellular microalgae, the homeostasis of this essential yet toxic metal could be regulated through storage vacuoles to minimize oxidative stress. In the host cell, Fe was localized in high concentrations in specific subcellular structures but was, on average, 2.5 times less concentrated (34 ± 6 ppm) than in the symbiotic microalgae. Variability in metal homeostasis between symbiotic and free-living forms was also found for cobalt. Co was not detected in the free-living symbionts although this metal was present in the culture medium (Table S2). By contrast, we detected Co in symbiotic microalgae (25 ± 17 ppm), specifically in the nucleus, some organelles and vacuole. In the latter cellular compartment, Co could be co-localized in high concentration (up to 400 ppm) with Fe (Figure 4F, Figure S4). In the host cell, Co was homogeneously distributed in the cytoplasm (e.g. nucleus, Golgi apparatus) and was present at higher concentration (68 ppm) than in symbionts. For manganese, we found that the concentration was higher in symbiotic microalgae (24 ± 8 ppm) than in the host cell (11 ± 4 ppm), but was similar in free-living cells (32 ± 16 ppm) (Figure 4E, Table S3).

Overall, the subcellular quantitative mapping of metals showed that the metal homeostasis of microalgae was dramatically altered in symbiosis, implying specific mechanisms by which the host takes up and transfers these key elements to intracellular symbionts. Fe deprivation is known to decrease carbon fixation, N assimilation and overall photosynthetic activity in microalgal cells [39]. We therefore hypothesize that the host provides Fe in order to satisfy the high needs of the well-developed photosynthetic apparatus and antioxidant proteins [37]. The exclusive presence of cobalt in the symbiotic stage in the algal nucleus and vacuoles raises questions on the biological role of this element in the partnership. In microalgae, Co can be the metal centre of important enzymes, such as carbonic anhydrase for C fixation [37], but also the metal ligand of the essential vitamin B12 (cobalamin). Yet, to fully interpret metal homeostasis changes, future molecular analyses should investigate the genes and proteins that are involved into the transport and regulation of metals in free-living and symbiotic microalgae.

High sulfur concentration in symbiotic microalgae

Enhanced intracellular photosynthetic activity performed by numerous plastids inevitably leads to the harmful production of reactive oxygen species (ROS) and implies the existence of antioxidant mechanisms. In microalgae, sulfur (S) metabolism plays a key role in antioxidant protection with the production of several S-containing compounds, such as glutathione, and dimethylsulfoniopropionate (DMSP), which are also key components of the global S cycle of the ocean [40,41]. Plastids have a central role in sulfate uptake and the production of DMSP [42–44]. It has been shown that the symbiont *Phaeocystis* can produce 100-fold more DMSP than free-living microalgae [7,45], consistent with the notion that production of this compound increases with photosynthesis [46]. Here, we showed that the S concentration in symbiotic microalgae (2400 ± 500 ppm) was 1.7 times higher than that of their host (1400 ± 300 ppm) but was similar to that of free-living microalgae (3200 ± 400 ppm) (Figure 5, Table S3). These concentrations may be

underestimated since small S-molecules can be lost during sample preparation [47]. In the microalgal cells, S was mainly contained in plastids and cytoplasmic vacuoles (Figure 5E,L, Figure S5). In symbiosis, the S content decreased in plastids and was mainly localized in vacuoles, which increased in size (1.5-2 μm in diameter) and contained up to 6.5 times more S than the plastids (compared to 2.5 times more in free-living cells). In these vacuoles, S was the major macronutrient, P was not present, and N very low, suggesting the absence of nucleic acids and phospholipids and a low amount of S-containing amino acids (Figure 5H,L). Based on previous evidence that DMSP is the main S-containing molecule in microalgal cells [48,49] (i.e., representing more than 50% of the total organic S), is stored in *Phaeocystis* vesicles [50] and is produced in high amounts by symbiotic *Phaeocystis*, we speculate that these S-rich vacuoles may contain DMSP. The antioxidant properties of DMSP could reduce the oxidative stress of symbiotic *Phaeocystis*, which would be consistent with the enhanced oxidative stress scavenging during photosynthesis revealed by our photophysiology measurements (NPQ parameter, Figure S2). The capacity to reduce sulfur and produce different S-containing compounds for intracellular antioxidant defence would enhance the suitability of microalgae to be symbionts. It may also partially explain why high DMSP-producing red plastid lineages such as haptophytes and dinoflagellates are prevalent photosymbionts in oceanic waters [51].

Conclusions

This study shows that microalgae can be radically transformed at the morphological and metabolic levels following their integration into a host cell, a process that has not previously been reported in other algal symbioses. Specifically, by combining nanoscale imaging techniques and photophysiology, we provide evidence that host cells engulf ecologically successful microalgal cells from the environment and subsequently block cell proliferation without preventing plastid division to optimize the photosynthetic machinery (multiplication of voluminous plastids and thylakoids) for high productivity. In plants, the multiplication of plastids has been recognized as a means of increasing the surface exchange with the environment, in particular to enhance CO_2 diffusion [52]. The structural and functional changes of symbiotic microalgae are also paralleled by specific modifications of the trophic micro-environment (e.g., Fe). Considering the numerous N-rich plastids per symbiont cell and the low availability of N in oceanic waters [25], the host must transfer a substantial quantity of N to their intracellular symbionts. The recognized capacity of acantharian hosts to heterotrophically feed on a variety of prey could represent an essential source of N to sustain the photosynthesis of its symbionts [53].

Overall, this study sheds light on the capacity of a heterotrophic host to exploit and engineer photosynthetic cells in the ocean, and paves the way for *omics* studies to fully understand the molecular mechanisms of this algal remodelling. Our findings challenge the common view of photosymbiosis as being mutualistic in nature. This Acantharia-*Phaeocystis* interaction could rather be considered as farming or inverted parasitism of microalgal cells where the host largely benefits from the symbiosis. This scenario is further supported by the fact that *Phaeocystis* cells cannot be grown after the symbiotic stage, do not divide within their host and are very likely

digested at the end of the life cycle of the host [7]. Available evidence suggests that the degree of host control seems to be less pronounced in other photosymbioses (e.g. reef invertebrates, foraminiferans) since the algal symbiont can divide within its host and can be grown in culture or survive in natural seawater after the symbiotic stage [6,54]. In an evolutionary context, similar traits found in symbiotic *Phaeocystis* have been reported in *Paulinella chromatophora*, a recent primary endosymbiosis, where photosynthetic organelles (chromatophores) are 15-20 times larger than free-living cyanobacteria [55,56]. The Acantharia-*Phaeocystis* symbiotic partnership could therefore reflect a possible route for plastid acquisition where metabolic control of the host preceded the genetic integration and led to the morphological transformation of the photosynthetic endosymbiont. Alternatively, the expansion of the photosynthetic machinery in *Paulinella* and *Phaeocystis* could represent a host constraint to increase the photosynthetic yield while controlling a small number of symbionts within their cell. A comparison with other abundant planktonic photosymbioses using high resolution imaging combined with transcriptomics and proteomics will certainly elucidate the different facets of microalgae in photosymbiosis and shed light on key evolutionary mechanisms in plastid acquisition.

Acknowledgements

This study and J.D. received funding from the European Union's Horizon 2020 research and innovation programme, under the Marie Skłodowska-Curie grant agreement 658442 (MSCA-IF-2014). J.D. was also supported by the LabEx GRAL (ANR-10-LABX-49-01) and Pôle CBS from the University of Grenoble Alpes. We are thankful for using the analytical facilities of the Centre for Chemical Microscopy (ProVIS) at UFZ Leipzig, which is supported by European Regional Development Funds (EFRE - Europe funds Saxony) and the Helmholtz Association. This research is also supported by EMBRC-France, whose French state funds are managed by the ANR within the Investments of the Future programme under reference ANR-10-INBS-02. We are grateful to the Roscoff Culture Collection for providing the cultures, John Dolan and the marine service crew (Guillaume de Liège) from the Laboratoire d'Océanographie of Villefranche-sur-Mer (CNRS, UPMC). We also thank Guy Schoehn from the electron microscopy platform facilities, Christine Moriscot for her technical assistance, and Ian Probert, Florin Musat, Chris Bowler and Arthur R. Grossman for critically reading the manuscript and suggesting substantial improvements. The authors acknowledge the support and use of resources from Instruct (a Landmark ESFRI project) and the ESRF for providing beamtime. This work used the platforms of the Grenoble Instruct centre (ISBG; UMS 3518 CNRS-CEA-UJF-EMBL) with support from FRISBI (ANR-10-INBS-05-02) and GRAL (ANR-10-LABX-49-01) within the Grenoble Partnership for Structural Biology (PSB). The electron microscope facility is supported by the Rhône-Alpes Region, the Fondation Recherche Medicale (FRM), the fonds FEDER, the Centre National de la Recherche Scientifique (CNRS), the CEA, the University of Grenoble Alpes (UGA), EMBL, and the GIS-Infrastructures en Biologie Sante et Agronomie (IBISA). E.M. is supported by the ANR Oceanomics programme (ANR-11-BTBR-0008). C.U. is supported by a joint UGA-ETH Zurich PhD grant in the

framework of the "Investissements d'avenir" programme (ANR-15-IDEX-02). G.F. is supported by the RGP0052 HFSP grant. P.-H. J and G.F. are supported by the CEA_DRF_impulsion (Fib-Bio) grant.

Author contributions

J.D. designed research, collected samples, interpreted results, and drafted the manuscript. N.M. assisted experimental design and supervised the work. B.G. and J.D. jointly performed the sample preparation for high resolution microscopy. H.S., G.V. and R.T. conducted nanoSIMS, ToF-SIMS and X-ray fluorescence imaging. H.S. and J.D. processed and interpreted nanoSIMS and ToFSIMS data. G.V. analyzed and interpreted the S-XRF data. S.M. maintained and provided the algal cultures, and S.B. and M.S. assisted with experiments. N.L.S., Y.S. and P.H.J. conducted FIB-SEM imaging and C.U. analyzed the data. J.L., J.J. and E.M. performed and interpreted lipidomics analyses. G.F. performed and analyzed photophysiology measurements. J.D., G.F. and N.M. wrote the manuscript.

Declaration of Interests

The authors declare no competing interests.

References

1. Keeling, P.J. (2004). Diversity and Evolutionary History of Plastids and Their Hosts the Tree of Eukaryotes. *American Journal of Botany* *91*, 1481–1493.
2. Embley, T.M., and Martin, W. (2006). Eukaryotic evolution, changes and challenges. *Nature* *440*, 623–630.
3. Ball, S., Colleoni, C., Cenci, U., Raj, J.N., and Tirtiaux, C. (2011). The evolution of glycogen and starch metabolism in eukaryotes gives molecular clues to understand the establishment of plastid endosymbiosis. *Journal of Experimental Botany* *62*, 1775–1801.
4. Karkar, S., Facchinelli, F., Price, D.C., Weber, A.P.M., and Bhattacharya, D. (2015). Metabolic connectivity as a driver of host and endosymbiont integration. *Proceedings of the National Academy of Sciences* *112*, 10208–10215.
5. de Vargas, C., Audic, S., Henry, N., Decelle, J., Mahe, F., Logares, R., Lara, E., Berney, C., Le Bescot, N., Probert, I., *et al.* (2015). Eukaryotic plankton diversity in the sunlit ocean. *Science (New York, N.Y.)* *348*, 1261605.
6. Decelle, J., Colin, S., and Foster, R.A. (2015). Photosymbiosis in Marine Planktonic Protists. In *Marine Protists* (Tokyo: Springer Japan), pp. 465–500.
7. Decelle, J., Probert, I., Bittner, L., Desdevises, Y., Colin, S., de Vargas, C., Galí, M., Simó, R., and Not, F. (2012). An original mode of symbiosis in open ocean plankton. *Proceedings of the National Academy of Sciences of the United States of America* *109*, 18000–5.
8. Caron, D.A. (2016). Ocean science: The rise of Rhizaria. *Nature* *532*, 444–445.
9. Biard, T., Stemmann, L., Picheral, M., Mayot, N., Vandromme, P., Hauss, H., Gorsky, G., Guidi, L., Kiko, R., and Not, F. (2016). In situ imaging reveals the biomass of giant protists in the global ocean. *Nature* *532*, 504–507.
10. Guidi, L., Chaffron, S., Bittner, L., Eveillard, D., Larhlimi, A., Roux, S., Darzi, Y., Audic, S., Berline, L., Brum, J.R., *et al.* (2016). Plankton networks driving carbon export in the oligotrophic ocean. *Nature* *532*, 465–470.
11. Caron, D.A., Michaels, A.F., Swanberg, N.R., and Howse, F.A. (1995). Primary productivity by symbiont-bearing planktonic sarcodines (Acantharia, Radiolaria, Foraminifera) in surface waters near Bermuda. *Journal of Plankton Research* *17*, 103–129.
12. Lampitt, R.S., Salter, I., and Johns, D. (2009). Radiolaria: Major exporters of organic carbon to the deep ocean. *Global Biogeochemical Cycles* *23*.
13. Irwin, A.J., and Oliver, M.J. (2009). Are ocean deserts getting larger? *Geophysical Research Letters* *36*, 1–5.
14. Probert, I., Siano, R., Poirier, C., Decelle, J., Biard, T., Tuji, A., Suzuki, N., and Not, F. (2014). *Brandtodinium* gen. nov. and *B.nutricula* comb. Nov. (Dinophyceae), a

- dinoflagellate commonly found in symbiosis with polycystine radiolarians. *Journal of Phycology* 50, 388–399.
15. Caron, D.A., Alexander, H., Allen, A.E., Archibald, J.M., Armbrust, E.V., Bachy, C., Bell, C.J., Bharti, A., Dyhrman, S.T., Guida, S.M., *et al.* (2017). Probing the evolution, ecology and physiology of marine protists using transcriptomics. *Nature Reviews Microbiology* 15, 6–20.
 16. Worden, A.Z., Follows, M.J., Giovannoni, S.J., Wilken, S., Zimmerman, A.E., and Keeling, P.J. (2015). Rethinking the marine carbon cycle: Factoring in the multifarious lifestyles of microbes. *Science* 347, 1257594.
 17. Smith, W.O., Codispoti, L.A., Nelson, D.M., Manley, T., Buskey, E.J., Niebauer, H.J., and Cota, G.F. (1991). Importance of *Phaeocystis* blooms in the high-latitude ocean carbon cycle. *Nature* 352, 514–516.
 18. Schoemann, V., Becquevort, S., Stefels, J., Rousseau, V., and Lancelot, C. (2005). *Phaeocystis* blooms in the global ocean and their controlling mechanisms: A review. *Journal of Sea Research* 53, 43–66.
 19. Zingone, A., Chrétiennot-Dinet, M.J., Lange, M., and Medlin, L. (1999). Morphological and genetic characterization of *Phaeocystis cordata* and *P. jahnii* (Prymnesiophyceae), two new species from the Mediterranean Sea. *Journal of Phycology* 35, 1322–1337.
 20. Wakefield, T.S., Farmer, M.A., and Kempf, S.C. (2000). Revised description of the fine structure of *in situ* “zooxanthellae” genus *Symbiodinium*. *The Biological Bulletin* 199, 76–84.
 21. Siano, R., Montresor, M., Probert, I., Not, F., and de Vargas, C. (2010). *Pelagodinium* gen. nov. and *P. béii* comb. nov., a dinoflagellate symbiont of planktonic foraminifera. *Protist* 161, 385–99.
 22. Genty, B., Briantais, J.M., and Baker, N.R. (1989). The relationship between the quantum yield of photosynthetic electron transport and quenching of chlorophyll fluorescence. *Biochimica et Biophysica Acta - General Subjects* 990, 87–92.
 23. Breitbarth, E., Wohlers, J., Kläs, J., LaRoche, J., and Peeken, I. (2008). Nitrogen fixation and growth rates of *Trichodesmium* IMS-101 as a function of light intensity. *Marine Ecology Progress Series* 359, 25–36.
 24. Bouman, H.A., Platt, T., Doblin, M., Figueiras, F.G., Gudmundsson, K., Gudfinnsson, H.G., Huang, B., Hickman, A., Hiscock, M., Jackson, T., *et al.* (2018). Photosynthesis-irradiance parameters of marine phytoplankton: Synthesis of a global data set. *Earth System Science Data* 10, 251–266.
 25. Moore, C.M., Mills, M.M., Arrigo, K.R., Berman-Frank, I., Bopp, L., Boyd, P.W., Galbraith, E.D., Geider, R.J., Guieu, C., Jaccard, S.L., *et al.* (2013). Processes and patterns of oceanic nutrient limitation. *Nature Geosci* 6, 701–710.
 26. Quigg, A., Irwin, A.J., and Finkel, Z. V (2011). Evolutionary inheritance of elemental

- stoichiometry in phytoplankton. Proceedings. Biological sciences / The Royal Society 278, 526–534.
27. Klausmeier, C.A., Litchman, E., Daufresne, T., and Levin, S.A. (2004). Optimal nitrogen-to-phosphorus stoichiometry of phytoplankton. *Nature* 429, 171–174.
 28. Arrigo, K.R. (2005). Marine microorganisms and global nutrient cycles. *Nature* 437, 343–348.
 29. Elser, J.J. (2012). Phosphorus : a limiting nutrient for humanity ? *Current Opinion in Biotechnology* 23, 833–838.
 30. Raven, J.A. (2013). RNA function and phosphorus use by photosynthetic organisms. *Frontiers in Plant Science* 4, 1–13.
 31. Miller, D.J., and Yellowlees, D. (1989). Inorganic Nitrogen Uptake by Symbiotic Marine Cnidarians: A Critical Review. *Proceedings of the Royal Society B: Biological Sciences* 237, 109–125.
 32. Koop, K., Booth, D., Broadbent, A., Brodie, J., Bucher, D., Capone, D., Coll, J., Dennison, W., Erdmann, M., Harrison, P., *et al.* (2001). ENCORE: The Effect of Nutrient Enrichment on Coral Reefs. Synthesis of Results and Conclusions. *Marine Pollution Bulletin* 42, 91–120.
 33. Li, M., Shi, X., Guo, C., and Lin, S. (2016). Phosphorus deficiency inhibits cell division but not growth in the dinoflagellate *Amphidinium carterae*. *Frontiers in Microbiology* 7, 1–11.
 34. Jahnke, J. (1989). The light and temperature dependence of growth rate and elemental composition of *Phaeocystis globosa* scherffel and *P. Pouchetii* (HAR.) Lagerh. in batch cultures. *Netherlands Journal of Sea Research* 23, 15–21.
 35. Karl, D.M. (2014). Microbially Mediated Transformations of Phosphorus in the Sea: New Views of an Old Cycle. *Annual Review of Marine Science* 6, 279–337.
 36. Thiel, V., and Sjövall, P. (2011). Using Time-of-Flight Secondary Ion Mass Spectrometry to Study Biomarkers. *Annual Review of Earth and Planetary Sciences* 39, 125–156.
 37. Morel, F.M.M., and Price, N.M. (2003). The biogeochemical cycles of trace metals in the oceans. *Science (New York, N.Y.)* 300, 944–947.
 38. Twining, B.S., and Baines, S.B. (2013). The Trace Metal Composition of Marine Phytoplankton. *Annual Review of Marine Science* 5, 191–215.
 39. Allen, A.E., LaRoche, J., Maheswari, U., Lommer, M., Schauer, N., Lopez, P.J., Finazzi, G., Fernie, A.R., and Bowler, C. (2008). Whole-cell response of the pennate diatom *Phaeodactylum tricornerutum* to iron starvation. *Proceedings of the National Academy of Sciences* 105, 10438–10443.
 40. Sunda, W., Kieber, D.J., Kiene, R.P., and Huntsman, S. (2002). An antioxidant function

- for DMSP and DMS in marine algae. *Nature* *418*, 317–320.
41. Simó, R. (2001). Production of atmospheric sulfur by oceanic plankton: Biogeochemical, ecological and evolutionary links. *Trends in Ecology and Evolution* *16*, 287–294.
 42. Giordano, M., Norici, A., and Hell, R. (2005). Sulfur and phytoplankton: acquisition, metabolism and impact on the environment. *New Phytologist* *166*, 371–382.
 43. Takahashi, H., Kopriva, S., Giordano, M., Saito, K., and Hell, R. (2011). Sulfur Assimilation in Photosynthetic Organisms: Molecular Functions and Regulations of Transporters and Assimilatory Enzymes. *Annual Review of Plant Biology* *62*, 157–184.
 44. Curson, A., Williams, B., Pinchbeck, B., Sims, L., Bermejo Martínez, A., Rivera, P., Kumaresan, D., Mercadé, E., Spurgin, L., Carrión, O., *et al.* (2018). DSYB catalyses the key step of dimethylsulfoniopropionate biosynthesis in many phytoplankton. *Nature Microbiology*.
 45. Gutierrez-Rodriguez, A., Pillet, L., Biard, T., Said-Ahmad, W., Amrani, A., Simó, R., and Not, F. (2017). Dimethylated sulfur compounds in symbiotic protists: A potentially significant source for marine DMS(P). *Limnology and Oceanography*.
 46. Simo, R., Archer, S.D., Pedros Alio, C., Gilpin, L., and Stelfox Widdicombe, C.E. (2002). Coupled dynamics of dimethylsulfoniopropionate and dimethylsulfide cycling and the microbial food web in surface waters of the North Atlantic. *Limnology and Oceanography* *47*, 53–61.
 47. Raina, J.B., Clode, P., Cheong, S., Bougoure, J., Kilburn, M.R., Reeder, A., Forêt, S., Stat, M., Beltran, V., Thomas-Hall, P., *et al.* (2017). Subcellular tracking reveals the location of dimethylsulfoniopropionate in microalgae and visualises its uptake by marine bacteria. *eLife*, 1–17.
 48. Matrai, P.A., and Keller, M.D. (1994). Total organic sulfur and dimethylsulpropionate in marine phytoplankton: intracellular variations. *Marine Biology* *119*, 61–68.
 49. Giordano, M., and Raven, J.A. (2014). Nitrogen and sulfur assimilation in plants and algae. *Aquatic Botany* *118*, 45–61.
 50. Orellana, M. V., Matrai, P.A., Janer, M., and Rauschenberg, C.D. (2011). Dimethylsulfoniopropionate storage in *Phaeocystis* (Prymnesiophyceae) secretory vesicles. *Journal of Phycology* *47*, 112–117.
 51. Decelle, J., Colin, S., and Foster, R.A. (2015). Photosymbiosis in Marine Planktonic Protists. In *Marine Protists: Diversity and Dynamics*, S. Ohtsuka, T. Suzuki, T. Horiguchi, N. Suzuki, and F. Not, eds. (Tokyo: Springer Japan), pp. 1–637.
 52. Xiong, D., Huang, J., Peng, S., and Li, Y. (2017). A few enlarged chloroplasts are less efficient in photosynthesis than a large population of small chloroplasts in *Arabidopsis thaliana*. *Scientific Reports* *7*, 1–12.
 53. Swanberg, N.R., and Caron, D.A. (1991). Patterns of sarcodine feeding in epipelagic

- oceanic plankton. *Journal of Plankton Research* 13, 287–312.
54. Decelle, J., Carradec, Q., Pochon, X., Henry, N., Romac, S., Mahé, F., Dunthorn, M., Kourlaiev, A., Voolstra, C.R., Wincker, P., *et al.* (2018). Worldwide Occurrence and Activity of the Reef-Building Coral Symbiont Symbiodinium in the Open Ocean. *Current Biology* 28, 3625–3633.e3.
 55. Singer, A., Poschmann, G., Mühlich, C., Valadez-Cano, C., Hänsch, S., Hüren, V., Rensing, S.A., Stühler, K., and Nowack, E.C.M. (2017). Massive Protein Import into the Early-Evolutionary-Stage Photosynthetic Organelle of the Amoeba *Paulinella chromatophora*. *Current Biology* 27, 2763–2773.e5.
 56. Nowack, E.C.M. (2014). *Paulinella chromatophora* - Rethinking the transition from endosymbiont to organelle. *Acta Societatis Botanicorum Poloniae* 83, 387–397.
 57. Johnson, X., Vandystadt, G., Bujaldon, S., Wollman, F.-A., Dubois, R., Roussel, P., Alric, J., and Béal, D. (2009). A new setup for in vivo fluorescence imaging of photosynthetic activity. *Photosynthesis Research* 102, 85–93.
 58. Maxwell, K., and Johnson, G.N. (2000). Chlorophyll fluorescence—a practical guide. *Journal of Experimental Botany* 51, 659–668.
 59. Kashiv, Y., Ii, J.R.A., Lai, B., Rose, V., and Vogt, S. (2016). Imaging trace element distributions in single organelles and subcellular features. *Nature Publishing Group*, 1–9.
 60. Moore, K.L., Schroder, M., Wu, Z., Martin, B.G.H., Hawes, C.R., McGrath, S.P., Hawkesford, M.J., Feng Ma, J., Zhao, F.-J., and Grovenor, C.R.M. (2011). High-Resolution Secondary Ion Mass Spectrometry Reveals the Contrasting Subcellular Distribution of Arsenic and Silicon in Rice Roots. *Plant Physiology* 156, 913–924.
 61. Smart, K.E., Smith, J.A.C., Kilburn, M.R., Martin, B.G.H., Hawes, C., and Grovenor, C.R.M. (2010). High-resolution elemental localization in vacuolate plant cells by nanoscale secondary ion mass spectrometry. *Plant Journal* 63, 870–879.
 62. Palsgard, E., Lindh, U., and Roomans, G.M. (1994). Comparative study of freeze-substitution techniques for X-ray microanalysis of biological tissue. *Microscopy Research and Technique* 28, 254–258.
 63. Bernal, M., Sanchez-Testillano, P., Risueno, M.D.C., and Yruela, I. (2006). Excess copper induces structural changes in cultured photosynthetic soybean cells. *Functional Plant Biology* 33, 1001–1012.
 64. Clode, P.L., and Marshall, A.T. (2003). Calcium associated with a fibrillar organic matrix in the scleractinian coral *Galaxea fascicularis*. *Protoplasma* 220, 153–161.
 65. Marshall, A.T., Clode, P.L., Russell, R., Prince, K., and Stern, R. (2007). Electron and ion microprobe analysis of calcium distribution and transport in coral tissues. *The Journal of experimental biology* 210, 2453–2463.
 66. Kashiv, Y., Austin, J.R., Lai, B., Rose, V., Vogt, S., and El-Muayed, M. (2016). Imaging

- trace element distributions in single organelles and subcellular features. *Scientific Reports* 6, 21437.
67. Lozic, I., Bartlett, C.A., Shaw, J.A., Iyer, K.S., Dunlop, S.A., Kilburn, M.R., and Fitzgerald, M. (2014). Changes in subtypes of Ca microdomains following partial injury to the central nervous system. *Metallomics* 6.
 68. Chandra, S. (2005). Quantitative imaging of subcellular calcium stores in mammalian LLC-PK epithelial cells undergoing mitosis by SIMS ion microscopy. *European Journal of Cell Biology* 84, 783–797.
 69. Perrin, L., Carmona, A., Roudeau, S., and Ortega, R. (2015). Evaluation of sample preparation methods for single cell quantitative elemental imaging using proton or synchrotron radiation focused beams. *J. Anal. At. Spectrom.*, 2525–2532.
 70. Maco, B., Cantoni, M., Holtmaat, A., Kreshuk, A., Hamprecht, F. a, and Knott, G.W. (2014). Semiautomated correlative 3D electron microscopy of in vivo-imaged axons and dendrites. *Nature protocols* 9, 1354–66.
 71. Fedorov, A., Beichel, R., Kalphaty-Cramer, J., Finet, J., Fillion-Robbin, J.-C., Pujol, S., Bauer, C., Jennings, D., Fennessy, F., Sonka, M., *et al.* (2012). 3D slicers as an image computing platform for thw quantitative imaging network. *Magnetic resonance imaging* 30, 1323–1341.
 72. Cignoni, P., Cignoni, P., Callieri, M., Callieri, M., Corsini, M., Corsini, M., Dellepiane, M., Dellepiane, M., Ganovelli, F., Ganovelli, F., *et al.* (2008). MeshLab: an Open-Source Mesh Processing Tool. Sixth Eurographics Italian Chapter Conference, 129–136.
 73. Cotte, M., Pouyet, E., Salomé, M., Rivard, C., De Nolf, W., Castillo-Michel, H., Fabris, T., Monico, L., Janssens, K., Wang, T., *et al.* (2017). The ID21 X-ray and infrared microscopy beamline at the ESRF: status and recent applications to artistic materials. *J. Anal. At. Spectrom.* 32, 477–493.
 74. Martinez-Criado, G., Villanova, J., Tucoulou, R., Salomon, D., Suuronen, J.P., Laboure, S., Guilloud, C., Valls, V., Barrett, R., Gagliardini, E., *et al.* (2016). ID16B: A hard X-ray nanoprobe beamline at the ESRF for nano-analysis. *Journal of Synchrotron Radiation* 23, 344–352.
 75. Solé, V.A., Papillon, E., Cotte, M., Walter, P., and Susini, J. (2007). A multiplatform code for the analysis of energy-dispersive X-ray fluorescence spectra. *Spectrochimica Acta - Part B Atomic Spectroscopy* 62, 63–68.
 76. Polerecky, L., Adam, B., Milucka, J., Musat, N., Vagner, T., and Kuypers, M.M.M. (2012). Look@NanoSIMS - a tool for the analysis of nanoSIMS data in environmental microbiology. *Environmental Microbiology* 14, 1009–1023.
 77. Vanbellinghen, Q.P., Elie, N., Eller, M.J., Della-Negra, S., Touboul, D., and Brunelle, A. (2015). Time-of-flight secondary ion mass spectrometry imaging of biological samples with delayed extraction for high mass and high spatial resolutions. *Rapid Communications*

- in Mass Spectrometry 29, 1187–1195.
78. Iverson, S.J., Lang, S.L.C., and Cooper, M.H. (2001). Comparison of the bligh and dyer and folch methods for total lipid determination in a broad range of marine tissue. *Lipids* 36, 1283–1287.
 79. Folch, J., Lees, M., and Sloane, G.H. (1957). A simple method for the isolation and purification of total lipides from animal tissues. *J. Biol. Chem.* 226, 497–509.
 80. Jouhet, J., Maréchal, E., Bligny, R., Joyard, J., and Block, M.A. (2003). Transient increase of phosphatidylcholine in plant cells in response to phosphate deprivation. *FEBS Letters* 544, 63–68.
 81. Jouhet, J., Lupette, J., Clerc, O., Magneschi, L., Bedhomme, M., Collin, S., Roy, S., Maréchal, E., and Rébeillé, F. (2017). LC-MS/MS versus TLC plus GC methods: Consistency of glycerolipid and fatty acid profiles in microalgae and higher plant cells and effect of a nitrogen starvation. *PLoS ONE* 12, 1–21.
 82. Demé, B., Cataye, C., Block, M.A., Maréchal, E., and Jouhet, J. (2014). Contribution of galactoglycerolipids to the 3-dimensional architecture of thylakoids. *FASEB Journal* 28, 3373–3383.
 83. Buseman, C.M. (2006). Wounding Stimulates the Accumulation of Glycerolipids Containing Oxophytodienoic Acid and Dinor-Oxophytodienoic Acid in Arabidopsis Leaves. *Plant Physiology* 142, 28–39.
 84. Rainteau, D., Humbert, L., Delage, E., Vergnolle, C., Cantrel, C., Maubert, M.A., Lanfranchi, S., Maldiney, R., Collin, S., Wolf, C., *et al.* (2012). Acyl chains of phospholipase D transphosphatidylation products in Arabidopsis cells: A study using multiple reaction monitoring mass spectrometry. *PLoS ONE* 7.

Figures legends

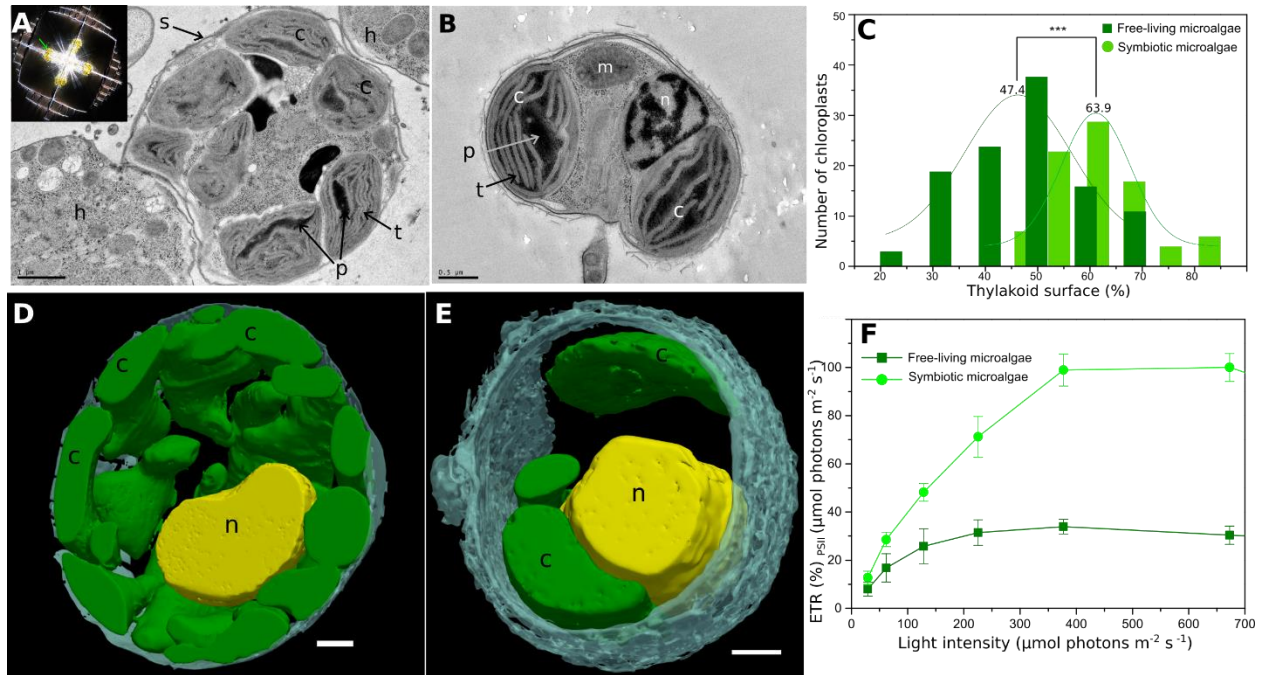


Figure 1. Morphological transformation of the microalga *Phaeocystis* between the free-living and symbiotic stages for enhanced photosynthesis.

(A) Ultrastructure of the symbiotic microalga *Phaeocystis cordata* within acantharian host unveiled by transmission electron microscopy (TEM). Scale bar = 1 μm . Inset: light microscopy image showing an acantharian host cell with its star-shaped biomineralized skeleton and its intracellular microalgae *Phaeocystis* (yellow cells indicated by a green arrow).

(B) Ultrastructure in TEM of the free-living *Phaeocystis* cell grown in culture with two parietal plastids. Scale bar = 0.5 μm . n: nucleus; c: plastid; p: pyrenoid; h: host; t: thylakoid membrane; s: symbiosome membrane; m: mitochondria.

(C) Surface occupied by thylakoid membranes per plastid in free-living (light green; 47.37% \pm 12.88, n = 113 plastids) and symbiotic (dark green, 63.85% \pm 8.95, n = 86 plastids) *Phaeocystis* calculated from TEM micrographs.

(D-E) 3D visualization with FIB-SEM (Focused Ion Beam Scanning Electron Microscopy) of the microalga *Phaeocystis* in symbiosis within a host (D) and in free-living phase (E) with plastids (green) and a nucleus (yellow). Scale bar = 1 μm . (See also Figure S1 and Video S1).

(F) Photosynthetic efficiency measured by the relative electron transfer rate (ETR) for free-living (dark green squares; 23 measures from a triplicate) and symbiotic (light green circles; 10 measures from a triplicate) microalgae over a range of light intensities up to 700 $\mu\text{mol photons m}^{-2} \text{s}^{-1}$. (See also Figure S2).

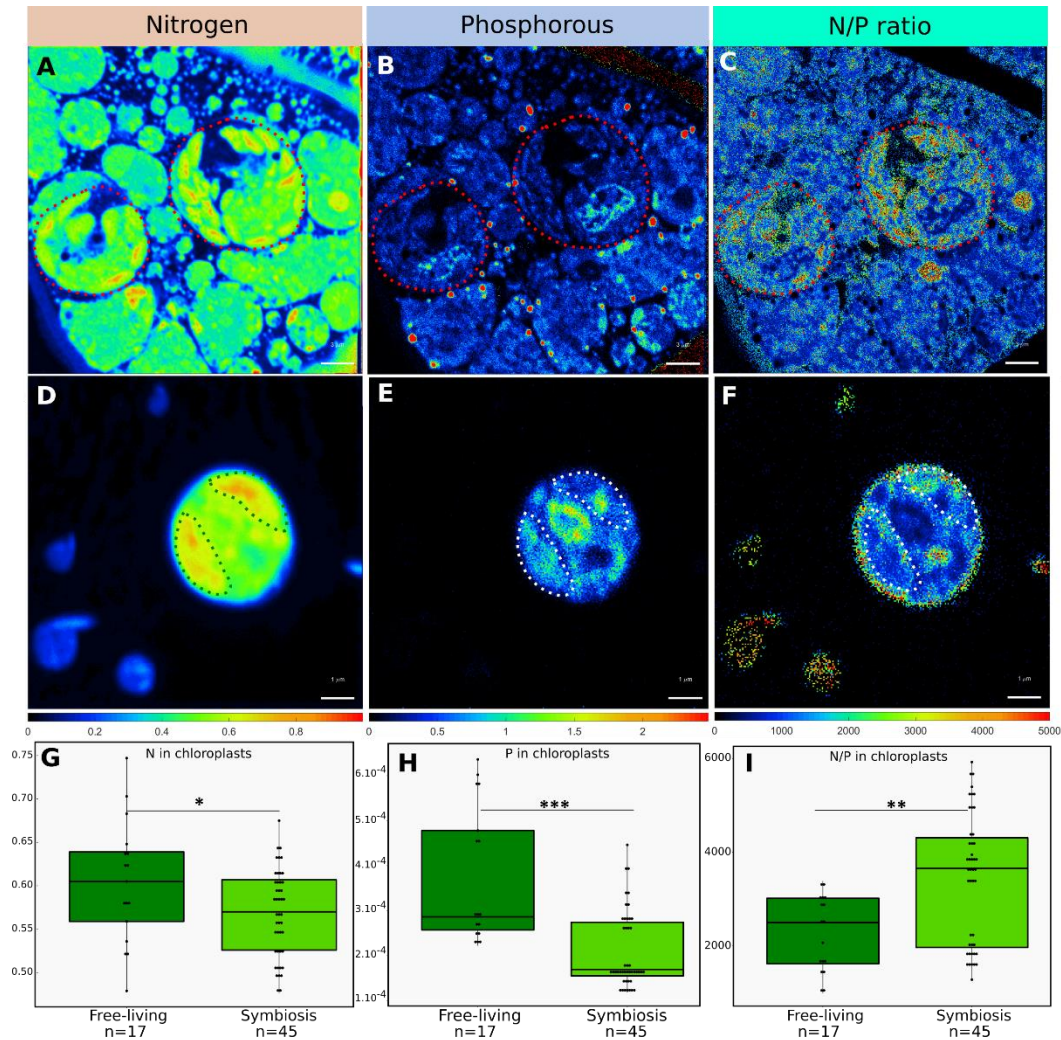


Figure 2. Subcellular quantitative mapping of nitrogen (N), phosphorous (P) and their stoichiometric ratios (N/P) in symbiotic and free-living *Phaeocystis* cells measured by nanoSIMS.

(A,B,C) Subcellular distribution of nitrogen ($^{12}\text{C}^{14}\text{N}/^{12}\text{C}_2$), phosphorous ($^{31}\text{P}^{16}\text{O}_2/^{12}\text{C}_2$) and the N/P ratio ($^{12}\text{C}^{14}\text{N}/^{31}\text{P}^{16}\text{O}_2$) in two symbiotic *Phaeocystis* algal cells highlighted by a red dashed line. Note that the two symbiotic microalgae are intracellular within their host cell. Scale bar = 3 μm .

(D,E,F) Subcellular distribution of nitrogen ($^{12}\text{C}^{14}\text{N}/^{12}\text{C}_2$), phosphorous ($^{31}\text{P}^{16}\text{O}_2/^{12}\text{C}_2$) and the N/P ratio ($^{12}\text{C}^{14}\text{N}/^{31}\text{P}^{16}\text{O}_2$) in one free-living *Phaeocystis* algal cell. The two plastids of the algal cell are highlighted by a green and white dashed line. Scale bar = 1 μm .

(G,H,I) Nitrogen ($^{12}\text{C}^{14}\text{N}/^{12}\text{C}_2$) and phosphorous ($^{31}\text{P}^{16}\text{O}_2/^{12}\text{C}_2$) content, and the N/P stoichiometric ratio ($^{12}\text{C}^{14}\text{N}/^{31}\text{P}^{16}\text{O}_2$) in plastids of free-living and symbiotic microalgae. (see also Data S1). Statistical analyses were performed using ANOVA type II tests based on 17 plastids of free-living microalgae and 45 plastids of symbiotic microalgae. $^{12}\text{C}^{14}\text{N}/^{12}\text{C}_2$ was log-transformed, and Tukey's Ladder for Power transformation was applied to $^{31}\text{P}^{16}\text{O}_2/^{12}\text{C}_2$ and $^{12}\text{C}^{14}\text{N}/^{31}\text{P}^{16}\text{O}_2$ (* $p < 0.05$, ** $p < 0.01$; *** $p < 0.001$, ANOVA test).

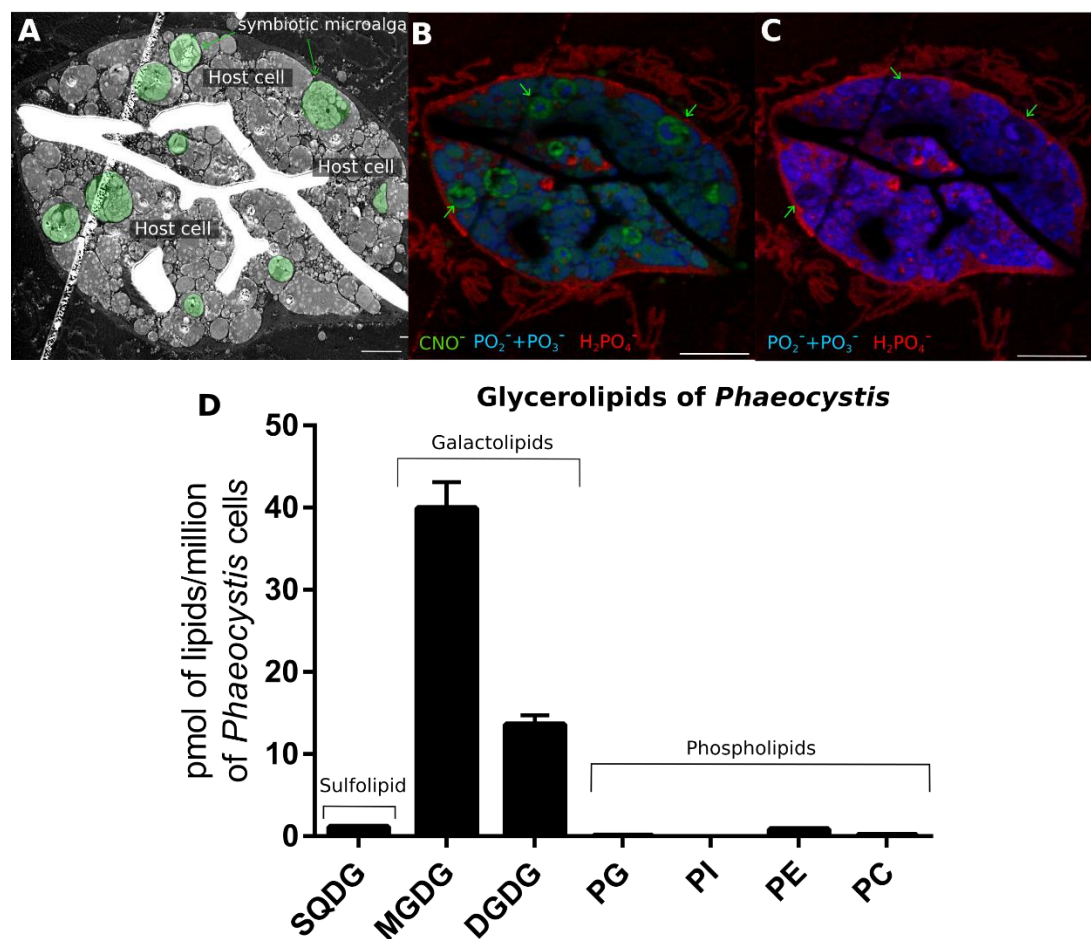


Figure 3. Subcellular distribution of phosphorous-containing molecules in the host Acantharia and lipid composition of the microalga *Phaeocystis*.

(A) Scanning electron microscopy (SEM) image of a host acantharian cell containing endosymbiotic microalgae *Phaeocystis* artificially coloured in green; Scale bar = 10 μm .

(B,C) Corresponding ToF-SIMS images of the whole host cell showing the subcellular distribution of the accumulated phosphate ions PO_2^- (m/z 62.98) and PO_3^- (m/z 78.96) in blue, in lower concentration in plastids of the symbiont *Phaeocystis* (highlighted by green arrows); in red, the ion fragment H_2PO_4^- (dihydrogen phosphate; m/z 96.96) located mainly in two cytoplasmic membranes of the host cell, and in green, nitrogen (CNO^- ; m/z 42.01) in high concentration in the symbiont plastids. Scale bar = 20 μm .

(D) Lipidomics analyses showing the composition of glycerolipids (sulfolipids, galactolipids and phospholipids) in the free-living *Phaeocystis* microalgae grown in culture medium. SQDG: sulfoquinovosyldiacylglycerol; MGDG and DGDG (mono- and digalactosyldiacylglycerol, respectively); PG: phosphatidylglycerol; PI: phosphatidylinositol; PE: phosphatidylethanolamine; PC: phosphatidylcholine.

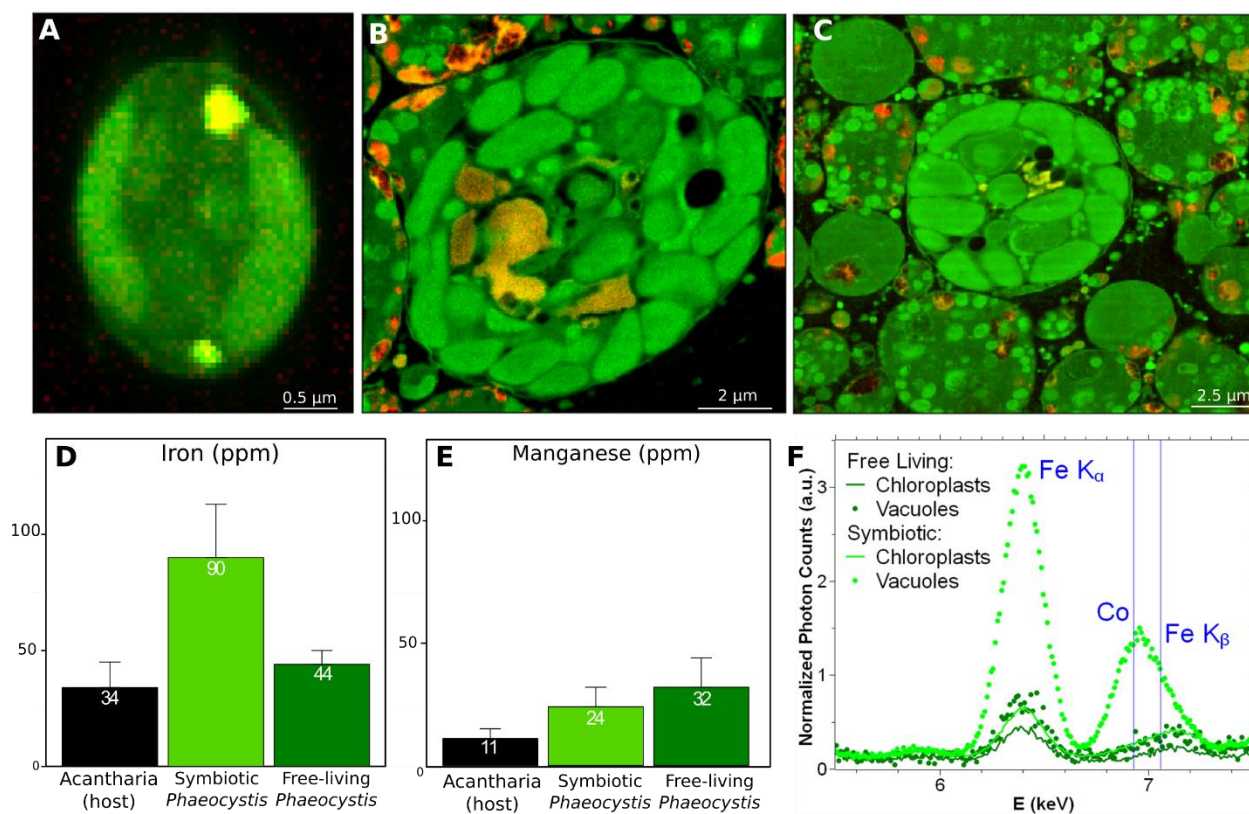


Figure 4. Subcellular distribution and quantification of trace metals (Fe, Mn, Co) in free-living and symbiotic microalgae by Synchrotron X-ray fluorescence (S-XRF).

(A) In free-living *Phaeocystis*, Fe (red) is localized in the two plastids and in vacuoles (osmium showing the ultrastructure is in green). The co-localization of Fe and Os is indicated by the yellow colour. (See also Tables S3 and S4, and Figure S4).

(B-C) In symbiosis, Fe concentration increases in *Phaeocystis* and is mainly stored in large vacuoles (yellow).

(D-E) Fe and Mn concentration in the host cells (black bars) and in the symbiotic and free-living *Phaeocystis* cells (light and dark green bars, respectively) (see also Table S3).

(F) Average S-XRF spectrum per pixel in subcellular compartments of *Phaeocystis* in free-living (light green) and symbiotic (dark green) stages, showing high Fe concentration in vacuoles of symbiotic microalgae (light green circles), where cobalt (Co) is also present (See also Table S4, and Figure S4).

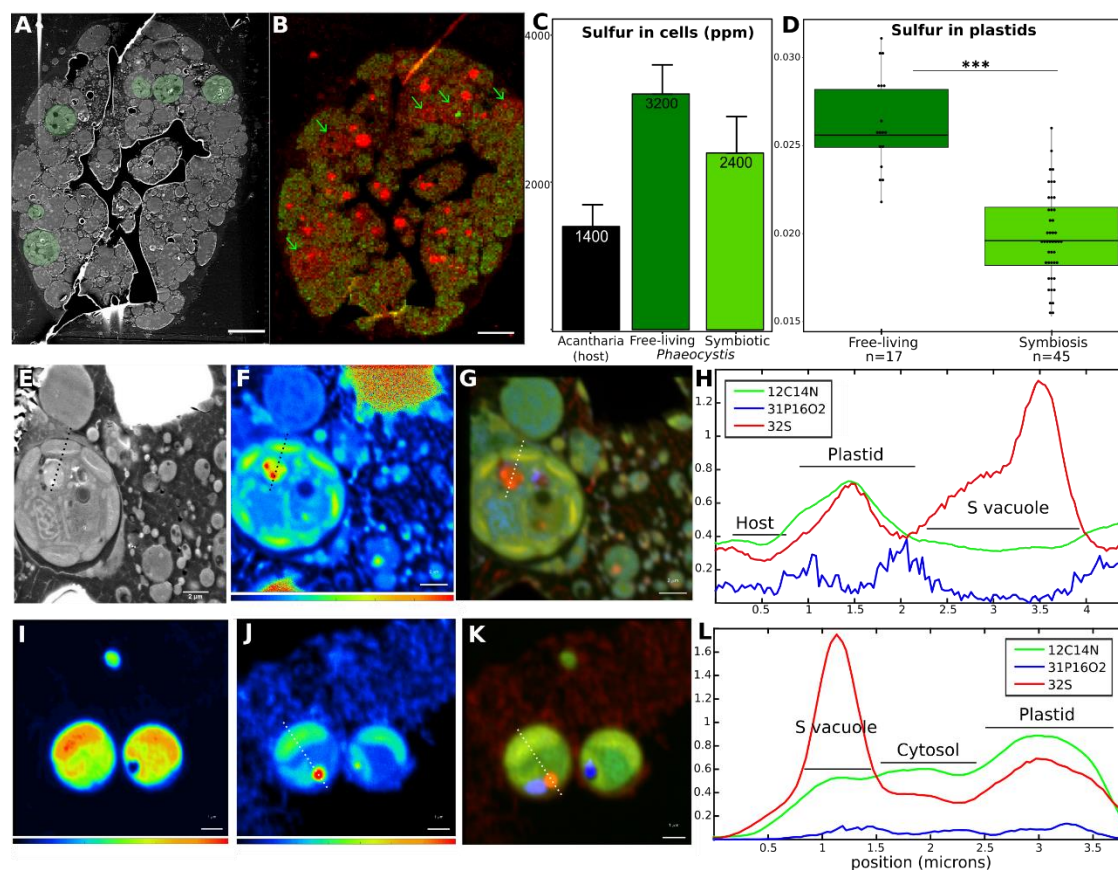


Figure 5. Subcellular distribution and quantification of sulfur in the symbiotic partners. (A) Scanning electron microscopy (SEM) images of the host-symbiont partnership (symbiotic microalgae *Phaeocystis* are artificially coloured in green).

(B) Correlated Synchrotron X-ray Fluorescence (S-XRF) mapping of sulfur (red) and phosphorous (green) showing high sulfur concentration in microalgae (indicated by green arrows). Scale bar = 20 μm .

(C) Sulfur concentration (ppm) measured by S-XRF in the host cell (dark bar) and the free-living and symbiotic *Phaeocystis* cells (dark and light green, respectively).

(D) Sulfur content ($^{32}\text{S}/^{12}\text{C}_2$) in plastids of free-living and symbiotic *Phaeocystis* measured by nanoSIMS. Statistical analyses were performed using ANOVA type II tests, and the $^{32}\text{S}/^{12}\text{C}_2$ was log-transformed (***) $p < 0.001$, ANOVA test). (See also Data S1).

(E) SEM image of a single symbiont cell with a bright round vacuole.

(F) Subcellular distribution of sulfur ($^{32}\text{S}^-$) in symbiotic *Phaeocystis*.

(G) RGB image showing the subcellular distribution of sulfur $^{32}\text{S}^-$ (red), nitrogen $^{12}\text{C}^{14}\text{N}^-$ (green) and phosphorous $^{31}\text{P}^-$ (blue) in symbiotic cells.

(H) Lateral profiling across the plastid and vacuole of the symbiotic microalga (dashed line in D, E and F) showing the contribution of the nutrients S, N and P (red, green and blue solid lines, respectively).

(I) Subcellular distribution of nitrogen ($^{12}\text{C}^{14}\text{N}^-$) in free-living *Phaeocystis*.

(J) Subcellular distribution of sulfur ($^{32}\text{S}^-$) in free-living *Phaeocystis*.

(K) RGB image showing the subcellular distribution of sulfur $^{32}\text{S}^-$ (red), nitrogen $^{12}\text{C}^{14}\text{N}^-$ (green) and phosphorous $^{31}\text{P}^-$ (blue) in free-living cells.

(L) Lateral profiling across the free-living microalga (dashed line in I and J) showing the contribution of S, N and P (red, green and blue solid lines, respectively).

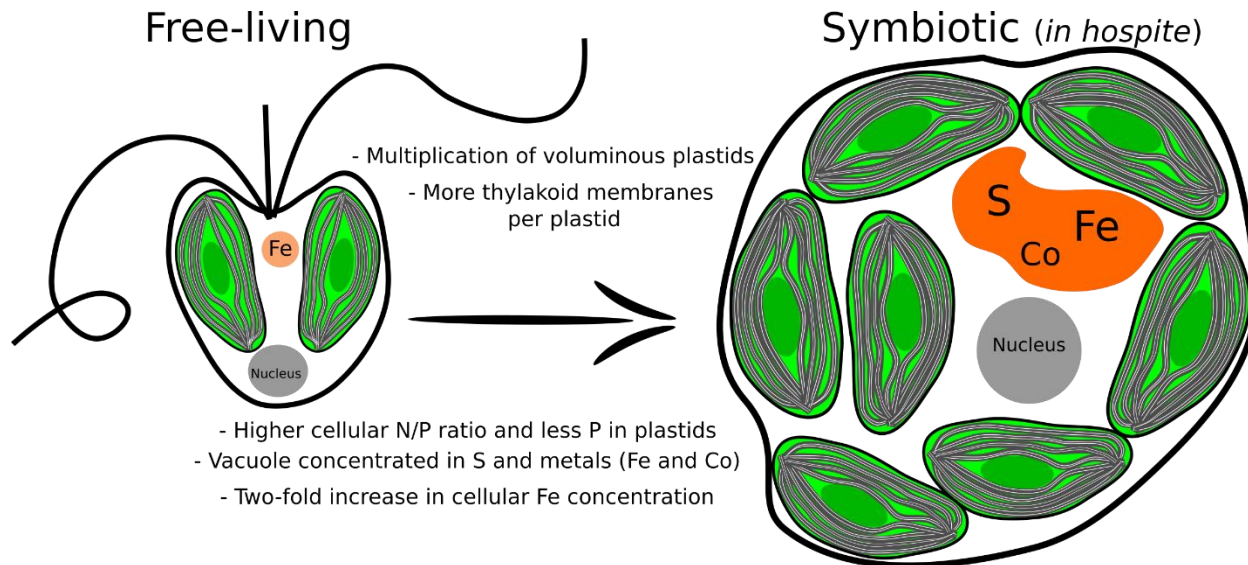


Figure 6. Schematic figure of the transition between free-living and symbiotic stages of the microalga *Phaeocystis* based on the results of this study.

STAR METHODS

CONTACT FOR REAGENT AND RESOURCE SHARING

Further information and requests for resources and reagents should be directed to and will be fulfilled by the Lead Contact, Johan Decelle (johan.decelle@univ-grenoble-alpes.fr).

EXPERIMENTAL MODEL AND SUBJECT DETAILS

Symbiotic acantharians harboring intracellular microalgal cells (*Phaeocystis*) were gently collected by towing a plankton net with a large cod-end (1 L) for 1-2 minutes in surface waters (Mediterranean Sea, Villefranche-sur-Mer, France). After collection, the individual cells were isolated under a microscope with a micropipette as in [7], rapidly transferred into natural seawater, and maintained in the same controlled light ($100 \mu\text{mol photons m}^{-2}\text{s}^{-1}$) and temperature (20°C) conditions as the free-living stage. In parallel, cultures of the haptophyte *Phaeocystis cordata* RCC 1383 (the symbiont of Acantharia in the Mediterranean Sea) [7] were maintained at 20°C in K/5 culture medium and at $100 \mu\text{mol photons m}^{-2}\text{s}^{-1}$. Nutrient concentrations of the free-living (culture medium K/5) and symbiotic (natural seawater surrounding the host) conditions of microalgae are provided in Table S2.

METHOD DETAILS

Photophysiology measurements

Photosynthetic parameters were derived from chlorophyll fluorescence emission measured in cultures of the microalga *Phaeocystis cordata* (free-living) (23 measures from a triplicate) and pools of 80-100 acantharian cells containing symbiotic *Phaeocystis* (10 measures from a triplicate). For measurements, we employed a fluorescence imaging setup previously described in [57]. The system was modified by replacing the green LEDs for actinic light with red LEDs (emission peak 630 nm, Full Width at Half Maximum 40 nm), and the acquisition setup was an ORCA flash 4.0 LT camera (Hamamatsu, Japan). The photosynthetic electron transfer rate, ETR_{PSII} , was calculated as the product of the light intensity times the photochemical yield in the light: $I * (F_m' - F) / F_m'$, where F and F_m' are the steady-state and maximum fluorescence intensities in light-acclimated cells, respectively, and I is the light irradiance in $\mu\text{mol quanta *m}^{-2} \text{s}^{-1}$ (see previous work [58] for more details). The light intensity was increased stepwise from 29 to $672 \mu\text{mol quanta *m}^{-2} \text{s}^{-1}$. At each light intensity, the cells were allowed to reaching steady state fluorescence emissions before increasing the photon flux. Photosynthesis (ETR) - irradiance curves were then fitted with an exponential saturation function to evaluate the maximum photosynthetic capacity (P_m), the initial slope (α : which is the photosynthetic efficiency under light levels close to zero), and the minimum photosynthetic saturation irradiance ($E_k = P_m / \alpha$) of free-living and symbiotic cells [24] (Table S1). The photoprotective responses were evaluated by measuring the non-photochemical quenching of fluorescence (NPQ [58]) using the fluorescence setup described above. The NPQ was calculated as $1 - (F_m' / F_m)$ where F_m is the maximum fluorescence emission in dark acclimated cells.

Sample preparation for electron microscopy and chemical imaging

Rapid freezing methods are recognized as superior to chemical fixation in preserving native-state cell ultrastructure and chemistry. Symbiotic acantharians (host and algal symbionts) and free-living microalgae in culture (*Phaeocystis cordata*) were therefore cryo-fixed using high-pressure freezing (HPM100, Leica) in which cells were subjected to a pressure of 210 MPa at -196°C , followed by freeze-substitution (EM ASF2, Leica). Prior to cryo-fixation, the microalgal cultures were concentrated by gentle centrifugation for 10 minutes. This cryo-preparation is recognized as the most suitable method to preserve the native chemistry of cells, including highly diffusible elements and trace elements [59–61]. For the freeze substitution (FS), a mixture of dried acetone and 1% osmium tetroxide was used. The FS machine was programmed as follows: 60-80 h at -90°C , heating rate of 2°C h^{-1} to -60°C (15 h), 10-12 h at -60°C , heating rate of 2°C h^{-1} to -30°C (15 h), and 10-12 h at -30°C . The cells were then washed several times in anhydrous acetone for 20 minutes at -30°C . Subsequently, the cells were gradually embedded in anhydrous araldite, a resin that contains negligible levels of the elements [62] and had been previously used in different analytical imaging studies [63–65]. A graded resin/acetone (v/v) series was used (30, 50 and 70% resin) with each step lasting 2 h at increased temperature: 30% resin/acetone bath from -30°C to -10°C , 50% resin/acetone bath from -10°C to 10°C , 70% resin/acetone bath from 10°C to 20°C . Samples were then placed in 100% resin for 8-10 h and in 100% resin with accelerator (BDMA) for 8 h at room temperature. Resin polymerization finally occurred at 65°C for 48 hours. The resin blocks and sections were stored in dry conditions before imaging. Prior to ultra-thin sectioning, symbiotic cells were observed in the resin block with a binocular and an inverted microscope to define the region of interest and the z-position of cells in the block, respectively. Trimming around the targeted cells was performed with razor blades and an EM Trimming Leica machine. Semi-thin sections (200-400 nm thick) were then obtained using an ultramicrotome (Leica EM) with an ultra-diamond knife (Diatome) and placed on 10-mm arsenic-doped silicon wafers for NanoSIMS and ToF-SIMS and on Si_3N_4 membrane windows for synchrotron X-ray fluorescence. Adjacent sections of 60- to 80-nm thick were also obtained for TEM analysis. Resin sections were rapidly collected on the water (< 30 sec) of the diamond knife. Because it has been shown that some diffusible molecules and elements can be lost at this step [66,67], we visualized the distribution of highly-diffusible elements (chlorine, potassium and calcium) with the synchrotron X-ray fluorescence (Figure S6). The presence of these mobile elements is a rule-of-thumb criterion to assess the chemical preservation of cells during the sample preparation [68,69].

Transmission Electron Microscopy (TEM) and Scanning Electron Microscopy (SEM)

For TEM analysis, ultrathin sections of 60 nm thickness were mounted onto copper grids or slots coated with formvar and carbon. Sections were then stained in 1% uranyl acetate (10 min) and lead citrate (5 min). Micrographs were obtained using a Tecnai G2 Spirit BioTwin microscope (FEI) operating at 120 kV with an Orius SC1000 CCD camera (Gatan). From the TEM images, the surface area occupied by the thylakoid membranes in plastids of symbiotic ($n = 86$ plastids) and free-living ($n = 113$ plastids) cells was calculated. To calculate this area, we performed a

manual area of interest extraction using GIMP software. By applying an adaptive thresholding technique, the pixels of the same greyscale were classified using computer vision library OpenCV linked to its python packages, and the classified pixels were computed for statistical analyses. Moreover, SEM was used to locate the cells on the sections, verify the quality of structural preservation, and identify the relevant regions of interest for subsequent chemical imaging with NanoSIMS, ToF-SIMS and S-XRF. The SEM micrographs were acquired at an electron energy of 5 kV using the secondary electron detector of the Zeiss Merlin VP Compact SEM at ProVIS.

Focused Ion Beam Scanning Electron Microscopy (FIB-SEM)

The sample was trimmed for FIB-SEM with a 90° diamond knife (Diatome) to expose cells at two surfaces (the imaging surface and the surface perpendicular to the focused ion beam, FIB) in order to optimize the acquisition [70]. After the sample was trimmed, it was mounted onto the edge of an SEM stub (Agar Scientific) using silver conductive epoxy (CircuitWorks) with the trimmed surfaces facing up and towards the edge of the stub. The sample was gold sputter coated (Quorum Q150RS; 180 s at 30 mA) and placed into the FIB-SEM for acquisition (Crossbeam 540, Carl Zeiss Microscopy GmbH). Once the ROI was located in the sample, Atlas3D software (Fibics Inc. and Carl Zeiss Microscopy GmbH) was used to perform sample preparation and 3D acquisitions. First, a 1- μm platinum protective coat (20 μm x 20 μm) was deposited with a 1.5 nA FIB current. The rough trench was then milled to expose the imaging cross-section with a 15 nA FIB current, followed by a polish at 7 nA. The 3D acquisition milling was done with a 1.5 nA FIB current. For SEM imaging, the beam was operated at 1.5 kV/700 pA in analytic mode using an EsB detector (1.1 kV collector voltage) at a dwell time of 8 μs with no line averaging. Datasets were acquired (8 nm pixel size and 8 nm steps) in z and aligned using the plugins StackReg provided by the open source software ImageJ. Dataset quality improvement and noise reduction were performed by 3D median filtering using the SciPy python package. The segmentation and 3D models of cells were performed using the 3D Slicer [71] and MeshLab [72] open source software packages.

Synchrotron X-ray fluorescence (S-XRF) imaging

S-XRF hyperspectral images were acquired on the ID21 and ID16B-NA beamlines of the European Synchrotron Radiation Facility [73,74]. Semi-thin sections (300 nm) were laid on Si_3N_4 membranes. On ID21, the incoming X-rays were tuned to the energy of 7.3 keV with a fixed-exit double crystal Si(111) monochromator and focused to $0.30 \times 0.75 \mu\text{m}^2$ with a Kirkpatrick-Baez (KB) mirror system, yielding a flux of $4.7 \cdot 10^{10}$ ph/s. The experiment was performed under vacuum (10^{-5} - 10^{-4} mbar). The emitted fluorescence signal was detected with energy-dispersive, large area (80 mm^2) SDD detectors equipped either with polymer or with Be window (XFlash 5100 from Bruker and SGX from RaySpec, respectively). Images were acquired by raster scanning the sample in the X-ray focal plane, with a $0.5 \times 0.5 \mu\text{m}^2$ step and a 1 s or 500 ms dwell time. The detector response was calibrated over a thin film reference sample consisting of layers of elements in ng/mm^2 concentration sputtered on a 200-nm thick Si_3N_4 membrane (RF7-200-S2371 from AXO), measured using the same acquisition parameters. Elemental mass fractions were calculated from

fundamental parameters with the PyMca software package[75], assuming a biological matrix of light elements only (H, C, N, O). For comparison between concentrations in different samples and sample areas (host vs symbiont, free-living vs symbiotic), we performed the acquisitions in identical experimental conditions (Be-window detector, fixed detector-sample distance, 300 nm cuts, 500 ms/pixel dwell time) to ensure the comparability of the results. Areas were chosen by manually selecting the pixels in the region of interest and summing up their fluorescence signal; the sum spectrum normalized by the number of pixels was then subjected to spectral deconvolution, and the peak areas were converted in mass fractions. Three sections per sample were analysed, and their average and standard deviation are reported in Table S3.

On ID16B-NA, a beam of 17.5 keV focused to 50×50 nm² through KB mirrors (2·10¹¹ ph/s) was used to excite X-ray fluorescence from the samples. High-resolution XRF images (50×50 nm² step size) were acquired in air, with a dwell time of 100 ms/pixel. Two 3-element SDD detector arrays were used to collect fluorescence from the sample. The detector response was calibrated over a thin film reference sample (RF8-200-S2453 from AXO). High-resolution images were acquired for free-living (n = 4) and symbiotic (n = 6) microalgae and in selected areas of the host (See also Table S4). Elemental quantification was extracted from fundamental parameters. To cross-check the consistency between data obtained with different experimental conditions (µm resolution and low excitation energy vs nm resolution and high energy, on ID21 and ID16B-NA, respectively), the estimated Fe concentrations in free-living *Phaeocystis* were compared: 44±6 ppm (ID21) and 50±5 ppm (ID16B-NA) lie within the error (See also Tables S3 and S4).

NanoSIMS acquisition and analyses

Semi-thin sections (200-300 nm) on silicon wafers were coated with 20-nm gold-palladium and analysed with a nanoSIMS 50L (Cameca, Gennevilliers, France) at the ProVIS Centre (UFZ Leipzig). A 16-keV Cs⁺ primary ion beam of 1–2 pA focused to approximately 70 nm was rastered over the sample area between 15×15 µm² and 70×70 µm² in size, with a dwelling time of 2 ms/pixel in a 512×512 or 1024×1024 pixel pattern, keeping the physical distance between pixels well below the beam size in order to avoid an ion beam induced surface roughening. The analysis areas were defined based on previous SEM observation. Before analysis, each area was pre-implanted with a 1 nA Cs⁺ ion beam for 1–2 min to equilibrate the yield of negative secondary ions. Multiple analysis scans (up to 100) were recorded for each area. Secondary ions extracted from each pixel of the sample surface were analysed for their mass to charge (m/z) ratio and counted separately with 7 electron multiplier detectors. The mass resolving power (MRP) of the spectrometer was set to 9000 ($M/\Delta M$) to resolve isobaric interferences. Different secondary ions (¹²C¹⁴N⁻, ³¹P or ³¹P¹⁶O₂, ³²S, ¹⁶O, ¹²C₂ or ¹²C) were detected in simultaneous collection mode by pulse counting to generate 10-100 serial maps of secondary ion count for their further quantitative evaluation. The analysed sample depth had been measured to be between 50 nm and 200 nm.

For each nanoSIMS secondary ion count map, the regions of interest (ROI) were defined by manual drawing with the look@nanosims software [76], and ion counts (normalized by scans and pixels number) and ratios were calculated for each ROI (Data S1, Figures S7 and S8). In total, nine microalgal cells in symbiosis from three different host cells were analysed. Four classes of ROIs

were defined: host cell, whole microalgal cell (*Phaeocystis*), cytosol and plastid of the microalgal cell. In addition, eleven microalgal cells in the free-living stage were analysed, where three ROIs classes were defined: entire cell, plastid of the alga and cytosol of the alga. Note that the cytosol of the microalgal cell can include the nucleus and vacuoles. In order to compare the relative N and P content between host, symbiotic and free-living microalgae, the total ions counts of elements (e.g. ^{31}P or $^{12}\text{C}^{14}\text{N}^-$) were normalized by the total ions counts of carbon (C_2). These analyses do not provide absolute quantification of N and P concentration but a comparison of the relative N and P content between ROIs of the algae and the host. For each ROI, the nitrogen, phosphorous and sulfur contents were therefore calculated by $^{12}\text{C}^{14}\text{N}/^{12}\text{C}_2$, $^{31}\text{P}^{16}\text{O}_2/^{12}\text{C}_2$ and $^{32}\text{S}/^{12}\text{C}_2$, respectively. Similarly, the stoichiometric ratio N/P was estimated by $^{12}\text{C}^{14}\text{N}/^{31}\text{P}^{16}\text{O}_2$. For comparison of different ROIs from the same acquisition, the homogeneity of variance was tested using Levene's test proposed in look@nanosims, and significant differences were tested using either the Kruskal-Wallis or ANOVA test. For cross-comparisons of different acquisitions, statistical significance was evaluated by performing ANOVAs with type II tests to account for unbalanced datasets. To meet the assumptions for ANOVA analysis, $^{12}\text{C}^{14}\text{N}/^{12}\text{C}_2$ was log-transformed, and Tukey's Ladder for Power transformation was applied to $^{31}\text{P}^{16}\text{O}_2/^{12}\text{C}_2$ and $^{12}\text{C}^{14}\text{N}/^{31}\text{P}^{16}\text{O}_2$. Confidence intervals were set to 95%. All statistical analyses were carried out using the R software (version 3.4.3, R Core Team 2017) with the packages 'car', 'DescTools' and 'rcompanion'.

ToF-SIMS acquisition and analyses

Qualitative analysis of molecular composition was performed on uncoated semi-thin sections, employing the time-of-flight secondary ion mass spectrometry technique (ToF-SIMS) with a ToF-SIMS.5 (ION-TOF GmbH, Münster) instrument. The ToF-SIMS experiment was performed using the imaging mode of ToF-SIMS.5 operation in combination with a delayed extraction [77] of negative secondary ions, providing a mass resolving power (MRP) above 3000 and a lateral resolution of approximately 150 nm. In these experimental conditions, the 30-keV NanoProbe LMIG source delivered 0.02 pA of primary Bi_{32}^+ cluster ions in 100 ns pulses with a 200 μs repetition period. The analysis has been done in 400 scans/plains with 5 shots of Bi_{32}^+ primary cluster ions per pixel distributed randomly in a 512x512 raster over a 56x56 μm^2 sample area. 30 keV Bi_3^+ ions from a NanoProbe source were employed for analysis. The 110- μs repetition period of primary ion pulse delivered 0.03 pA of Bi_3^+ . The analysis was performed by rastering the primary ion beam randomly in a 1024x1024 pixels pattern over a 110x110 μm^2 sample area. Each shot of analysis Bi_3^+ ion beam was followed by sample charge compensation implemented with 12 eV electrons from flooding e-gun and 2×10^{-7} mbar partial pressure of Ar gas in the analysis chamber. The data were acquired in 306 planes. Each data plane was generated after 5 scans over the analysis area with 5 shots per pixel, and 5 keV [Ar]1757 cluster ions from a GCIB source were used for sample sputtering in non-interlaced mode. The accumulation of acquired scans/plains was done after lateral drift correction, and the resulted total stack was analysed for lateral distribution of ion yield using the SurfaceLab 6.7 software (ION-TOF GmbH).

Lipidomics analyses

Cultures of *Phaeocystis cordata* were concentrated, cryofixed and lyophilized. Total lipids were extracted by the Folch method [78,79]. Total glycerolipids were quantified from their fatty acids: in an aliquot fraction of extracted lipids, a known quantity of 15:0 was added, and the fatty acids were converted into methyl esters (FAME) by a 1 hour incubation in 3 mL of 2.5% H₂SO₄ in pure methanol at 100°C [80]. The reaction was stopped by the addition of 3 mL of water and 3 mL of hexane. The hexane phase was analysed using a gas chromatography-flame ionization detector and mass spectrometry (GC-FID/MS) (Perkin Elmer) on a BPX70 (SGE) column. FAME were identified by mass spectrometry and quantified by the surface peak method of the FID signal using 15:0 for calibration. For quantification of each lipid class by LC-MS/MS analysis, a fraction of extracted lipids corresponding to 25 nmol was resuspended in 100 µL of chloroform/methanol (2:1 v/v) containing 125 pmol of internal standards and analysed as described in [81] or the total extract was re-suspended in 40 µL of chloroform/methanol (2:1 v/v) containing 50 pmol of internal standards. Internal standard used for DAG, TAG, MGDG and DGDG was DAG 18:0-22:6 from Avanti Polar Lipid. The internal standard for PE was PE 18:0-18:0 from Avanti Polar Lipid, and the internal standard for PC, PI, PS, PA, DPG, PG and SQDG was SQDG 16:0-18:0 extracted from spinach thylakoid [82] and hydrogenated as described before [83]. Lipids were then separated by HPLC and quantified by MS/MS. The high-performance liquid chromatography (HPLC) separation method was adapted from a previous study [84]. Lipid classes were separated using an Agilent 1200 HPLC system using a 150 mm×3 mm (length × internal diameter) 5-µm diol column (Macherey-Nagel) at 40°C. The mobile phases consisted of hexane/isopropanol/water/ammonium acetate 1 M, pH 5.3 [625/350/24/1, (v/v/v/v)] (A), and isopropanol/water/ammonium acetate 1 M, pH 5.3 [850/149/1, (v/v/v)] (B). The injection volume was 20 µL. After 5 min, the percentage of B was increased linearly from 0% to 100% over 30 min and stayed at 100% for 15 min. This elution sequence was followed by a return to 100% A in 5 min and an equilibration for 20 min with 100% A before the next injection, leading to a total run time of 70 min. The flow rate of the mobile phase was 200 µL/min. The distinct glycerolipid classes were eluted successively as a function of the polar head group. Mass spectrometric analysis was done on a 6460 triple quadrupole mass spectrometer (Agilent) equipped with a Jet stream electrospray ion source under the following settings: drying gas heater, 260°C; drying gas flow 13 L.min⁻¹; sheath gas heater, 300°C; sheath gas flow; 11 L.min⁻¹; nebulizer pressure, 25 psi; capillary voltage, ± 5000 V; nozzle voltage, ± 1000. Nitrogen was used as collision gas. The quadrupoles Q1 and Q3 were operated at widest and unit resolution respectively. PC, DGTA and DGCC analysis were carried out in positive ion mode by scanning for precursors of m/z 184, 236 and 104 at collision energies (CE) of 34 eV, 52 eV and 40 eV, respectively. SQDG analysis was carried out in negative ion mode by scanning for precursors of m/z -225 at a CE of -56 eV. PE, PI, PG, MGDG and DGDG measurements were performed in positive ion mode by scanning for neutral losses of 141 Da, 277 Da, 189 Da, 179 Da and 341 Da at CEs of 20 eV, 12 eV, 16 eV, 8 eV and 8 eV, respectively. Quantification was performed using multiple reaction monitoring (MRM) with a 40-ms dwell time. Mass spectra were processed by MassHunter Workstation software (Agilent) for the identification and quantification

of lipids. Lipid amounts (pmol) were corrected for response differences between internal standards and endogenous lipids and by comparison with a quality control (QC). The QC extract corresponded to a known *Phaeodactylum tricornutum* lipid extract qualified and quantified by TLC and GC-FID as previously described [81].

QUANTIFICATION AND STATISTICAL ANALYSIS

Statistical analysis and graph production were performed using R with specific libraries mentioned above. For nanoSIMS data, the homogeneity of variance was tested using Levene's test proposed in the software look@nanosims, and significant differences were tested using either the Kruskal-Wallis or ANOVA test. For cross-comparisons of different nanosims acquisitions, statistical significance was evaluated by performing ANOVAs with type II tests to account for unbalanced datasets based on 17 plastids of 12 free-living microalgae and 45 plastids of 10 symbiotic microalgae. To meet the assumptions for ANOVA analysis, $^{12}\text{C}^{14}\text{N}/^{12}\text{C}_2$ was log-transformed, and Tukey's Ladder for Power transformation was applied to $^{31}\text{P}^{16}\text{O}_2/^{12}\text{C}_2$ and $^{12}\text{C}^{14}\text{N}/^{31}\text{P}^{16}\text{O}_2$. Confidence intervals were set to 95%. Statistical analyses were carried out using the R software (version 3.4.3, R Core Team 2017) with the packages 'car', 'DescTools' and 'rcompanion'. For the photophysiology measurements, 23 measures were conducted on cultures of free-living *Phaeocystis* in triplicate, and 10 measures on three pools of 80-100 acantharian cells containing symbiotic *Phaeocystis* (triplicate). Samples for lipidomics analyses were composed of two biological and three technical replicates. Synchrotron X-ray fluorescence was performed on 21 free-living *Phaeocystis* cells and 11 symbiotic *Phaeocystis* cells from three different host cells (Table S3). On the high resolution S-XRF beam line, four free-living and six symbiotic microalgae were also analyzed (See also Table S4).

Legends for the Supplemental Data and Video

Video S1. 3D models of the microalga *Phaeocystis* in free-living and in symbiotic condition within acantharian host. Related to Figure 1.

3D models of the free-living (left) and symbiotic (right) stages were reconstructed based on stacked images acquired with FIB-SEM (Focus Ion Beam Scanning Electron Microscope) with plastids (green) and nucleus (yellow).

Data S1. NanoSIMS data of the quantitative mapping of nitrogen (N), phosphorous (P) and sulfur (S) in host and microalgal cells, and their stoichiometric ratios. Related to Figures 2 and 5.

For each region of interest (ROI) of different host and algal cells (cytosol, chloroplast, the whole cell), the nitrogen, phosphorous and sulfur contents were calculated by $^{12}\text{C}^{14}\text{N}/^{12}\text{C}_2$, $^{31}\text{P}^{16}\text{O}_2/^{12}\text{C}_2$ and $^{32}\text{S}/^{12}\text{C}_2$, respectively. Similarly, the stoichiometric ratio N/P was estimated by $^{12}\text{C}^{14}\text{N}/^{31}\text{P}^{16}\text{O}_2$.

